

Pulse Electrodeposition of Manganese Oxide for High-Rate Capability Supercapacitors

Fang Xiao, Youlong Xu*

Electronic Materials Research Laboratory, Key Laboratory of the Ministry of Education, Xi'an Jiaotong University, No. 28, West Xianning Road, Xi'an 710049, China

*E-mail: xfang6321@gmail.com; ylxujtu@mail.xjtu.edu.cn

Received: 21 June 2012 / Accepted: 16 July 2012 / Published: 1 August 2012

Two kinds of manganese oxide films (denoted as p-MnO_x and g-MnO_x) were electrodeposited on graphite substrate by the pulse current or galvanostatic methods, respectively. The g-MnO_x showed Mn₃O₄ characteristics and the p-MnO_x exhibited a mixture of Mn₃O₄ and MnOOH phase from XRD pattern and Raman spectra. The g-MnO_x showed the capacitance of 160 F g⁻¹ while p-MnO_x exhibited 252 F g⁻¹ at the scanning rate of 10 mV s⁻¹. Interestingly, the retained ratio of capacitance of g-MnO_x was 31% whereas that of p-MnO_x was still 56% when the scanning rate increased to 500 mV s⁻¹. The high-rate capability of p-MnO_x may be primarily attributed to the improvement in wettability on the interface of electrode/electrolyte, which came from its more amount of hydroxyl, resulting in easier cation ions transport and more accessible active sites.

Keywords: Manganese oxides; Electrodeposition; Electrode materials; Supercapacitors.

1. INTRODUCTION

Supercapacitors are extensively studied as auxiliary energy storage devices to be used with rechargeable batteries [1]. It has been reported that supercapacitors with a ruthenium oxide electrode exhibit a large specific capacitance (SC) of as high as 720 F g⁻¹ [2]. However, the commercial application of ruthenium oxide is limited because of its expensive price, toxicity, and requires the use of a strong acidic electrolyte such as sulfuric acid. In order to develop alternative materials, activated carbons, transition metal oxides, and electronically conductivity polymers have been studied widely [3-5]. Among them, manganese oxide has attracted considerable attention in the supercapacitors due to its low-cost, friendly environment, and good electrochemical performances [6, 7].

Manganese oxide has been prepared by the various approaches, such as chemical precipitate [8], pyrogenation [9], sol-gel [10], mechanical grinding [11], hydrothermal synthesis [12] and

electrochemical deposition [13]. Since electrochemical deposition is clean, controllable and simple technique, many investigations have been focused on the electrochemical deposition of manganese dioxide films [14, 15]. Electrochemical deposition has various methods, including galvanostatic, potentiostatic, potentiodynamic and pulse deposition. Pulse deposition as one of important techniques has been widely applied to synthesize different thin films [16-18]. It can control chemical-physical properties of materials (such as morphology, electrical conductivity, porosity, adhesion, and compound content) through modifying pulse parameters [19]. Zhitomirsky and Jacob have prepared manganese oxide films using pulse or reverse pulse electrodeposition from KMnO_4 solutions and found that these films had higher capacitance due to their highly porous nanostructure [20]. Additionally, Ghaemi and Adelkhani have also found that manganese dioxide deposited by pulse current showed higher specific capacitance because of its higher level of cation vacancy, water content and porosity [21]. However, power characteristic is important for application of supercapacitors.

In this work, the manganese oxide films (denoted as p- MnO_x and g- MnO_x) were electrodeposited by the pulse current or galvanostatic methods from manganese acetate solutions, respectively. The characteristics of MnO_x films were examined by scanning electron microscope, X-ray diffraction (XRD), Raman spectra, X-ray photoelectron spectroscopy (XPS), contact angle, electrochemical impedances and cyclic voltammograms (CV).

2. EXPERIMENTAL

2.1 Synthesis.

Graphite slices (area: $1\text{cm} \times 2\text{cm}$) were chosen as substrates for the electrochemical depositions. The substrates were firstly polished with SiC paper of 1000 grit, degreased with acetone and water, then etched in a 0.5 mol L^{-1} H_2SO_4 solution for 10 min, and finally washed with water in an ultrasonic bath. All MnO_x films were electrodeposited in a neutral 0.25 mol L^{-1} $\text{Mn}(\text{CH}_3\text{COO})_2$ solution at $25 \pm 1^\circ\text{C}$. The electrochemical cell for deposition included the graphite substrates, a platinum counter electrode and a saturated calomel reference electrode (SCE). Pulse current deposition was conducted on with on-time of 0.25 s, off-time of 0.5 s, current density of 25 mA cm^{-2} and 7200 deposition cycles. Galvanostatic deposition was performed at the same current density during 30 min. The obtained samples were washed with deionized water, dried at 50°C in vacuum for 12 h.

2.2 Characterization.

The surface morphologies were examined by a field-emission scanning electron microscope (JEOL JSM-6700F). XRD patterns were recorded by X'Pert PRO (PANalytical Ltd.) with a $\text{Cu K}\alpha$ X-ray source ($\lambda = 1.5418\text{ nm}$) in the region of $20 - 80^\circ$. The Raman spectra were taken at room temperature in the spectral range $200 - 750\text{ cm}^{-1}$ using a LabRAMhr 800 (HORIBA JOBIN YVON) Raman microscope system. XPS analysis was performed on a Kratos Axis Ultra-DLD system, using $\text{Al K}\alpha$ radiation (1486.6 eV , pass energy of 10.0 eV). The contact angles of water on MnO_x films were

measured by a contact angle goniometer (Shanghai Solon, SL200B). The mass of deposited film was measured using electronic balance AG135 (Mettler Toledo, with 0.01 mg sensitivity). Electrochemical measurements were carried out by the Versatile Multichannel Potentiostat (Princeton Applied Research, VMP2/Z) using the three-electrode cell in 3 mol L⁻¹ KCl solution. The impedance data were analyzed and modeled using ZSimpWin V 3.20 of EChem Software.

3. RESULTS AND DISCUSSION

The morphologic photographs of g-MnO_x and p-MnO_x are shown in Fig. 1. The g-MnO_x in Fig. 1a exhibits rough surface with many cracks, which were probably caused by shrinkage stress during drying. Whereas the morphology of p-MnO_x (in Fig.1b) is relatively compact and well covered with spherical grains of uniform size (about 500nm). The results demonstrate that pulse current deposition causes the morphology of MnO_x to be more regular and more compact.

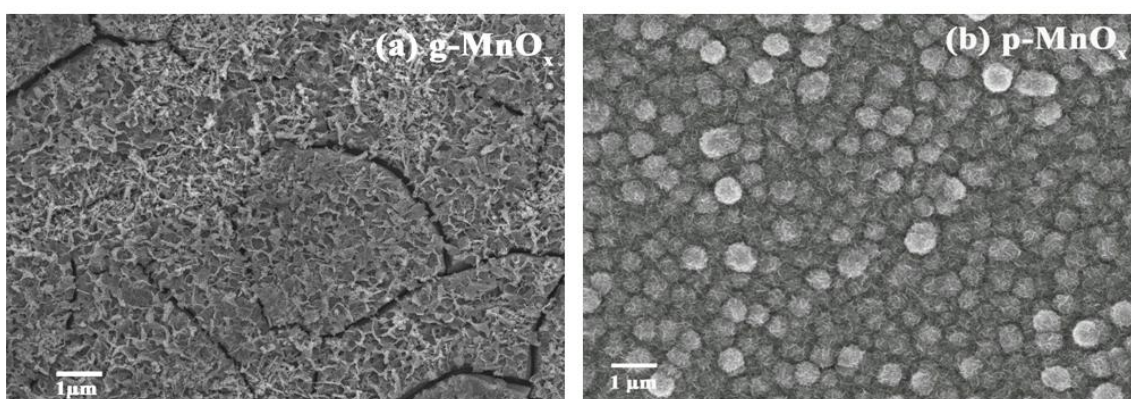


Figure 1. SEM photographs: (a) g-MnO_x and (b) p-MnO_x

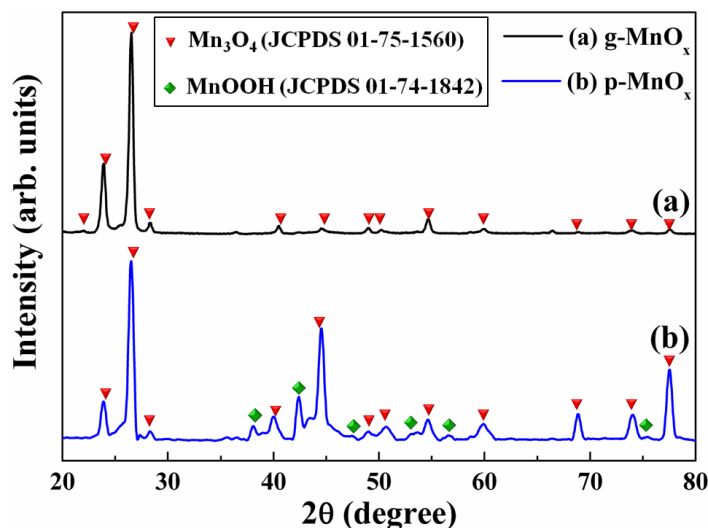


Figure 2. XRD patterns: (a) g-MnO_x and (b) p-MnO_x

The XRD patterns of g-MnO_x and p-MnO_x were shown in Fig.2. The reflection of the XRD pattern of g-MnO_x (in Fig.2a) is indexed to tetragonal phase of Mn₃O₄ (JCPDS 01-75-1560). However, the diffraction peaks on XRD pattern of p-MnO_x can be indexed to two structures of manganese oxides, i.e., tetragonal Mn₃O₄ (JCPDS 01-75-1560) and orthorhombic MnOOH (JCPDS 01-74-1842) (in Fig.2b). Pulse current method probably generates high instantaneous current densities, leading to very high positive potentials at the interface of electrode/electrolyte [19, 22]. Therefore, the higher valence of the p-MnO_x should be attributed to high positive potentials. Because the on-time of pulse current was very short, the p-MnO_x was mixture consisting of Mn₃O₄ and MnOOH.

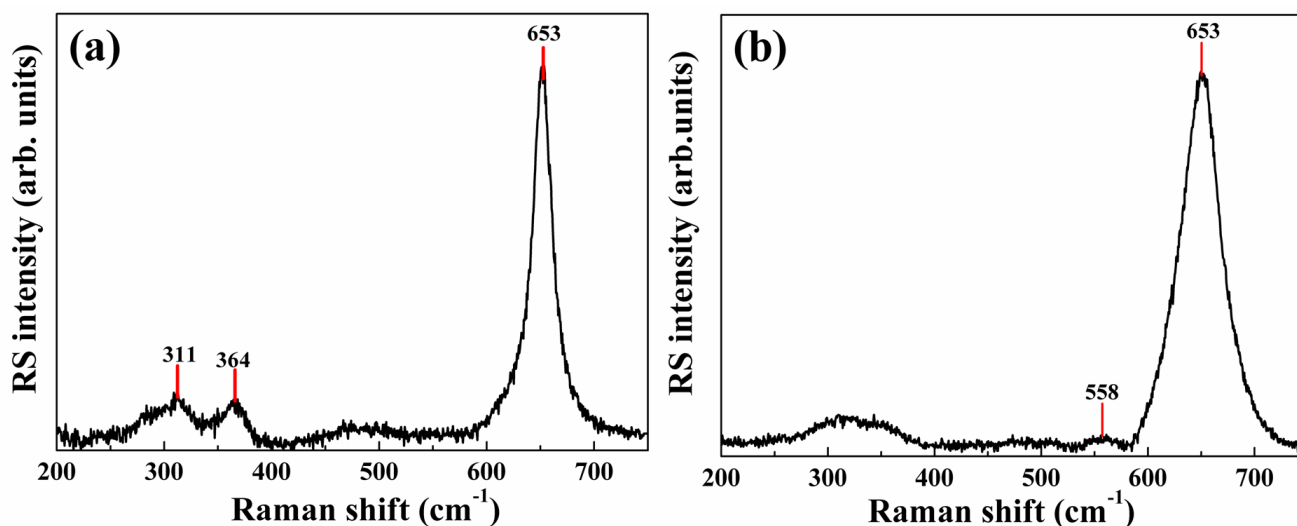


Figure 3. Raman spectra: (a) g-MnO_x and (b) p-MnO_x

Raman spectroscopy is an effective technique to investigate structure characteristics and chemical composition for manganese oxide. Fig.3 showed Raman spectra of the g-MnO_x and p-MnO_x. The Raman spectrum of g-MnO_x shows peaks at 311, 364 and 653 cm⁻¹ (in Fig.3a), which are in good agreement with those of Mn₃O₄ [23, 24]. The strongest peak at 653 cm⁻¹ corresponds to the Mn-O breathing vibration of divalent Mn ions in tetrahedral coordination [23]. The weaker peaks at 311 cm⁻¹ and 364 cm⁻¹ are correspond to the out-of-plane bending modes of Mn-O [25] and the asymmetric stretch of bridge oxygen species (Mn-O-Mn) [26], respectively. However, the Raman spectra of p-MnO_x (in Fig.3b) displays a sharp peak at 653 cm⁻¹, bands with weak intensity at 558 cm⁻¹ and a broad band from 260 to 390 cm⁻¹. The peak at 558 cm⁻¹ which is attributed to the stretching modes of MnO₆ octahedra, is assigned to MnOOH [23, 24]. The broad band may be formed due to the overlap of these characteristic peaks corresponding to Mn₃O₄ and MnOOH [27, 28].

MnO_x samples were characterized further using XPS analysis. In Fig.4 (a), two MnO_x samples show same binding energy of Mn 2p_{1/2} at 653.7 eV. The Mn 2p_{3/2} peaks of g-MnO_x and p-MnO_x position at 642.0 eV and 642.1 eV, respectively. Higher oxidation state of manganese denotes higher binding energy [29, 30]. The Mn 2p_{3/2} of p-MnO_x is slightly shifted to the higher binding energy side due to presence of MnOOH in p-MnO_x. Moreover, the Mn 2p spectrum of p-MnO_x displayed a distinct

shoulder peak between 645 and 646 eV in Fig.4 (a) (i.e., this peak indicated by arrows). This shoulder peak may be attributed to trivalent Mn ions of MnOOH in p-MnO_x. The Mn3s core level spectra of MnO_x samples also shows in Fig.4 (b).

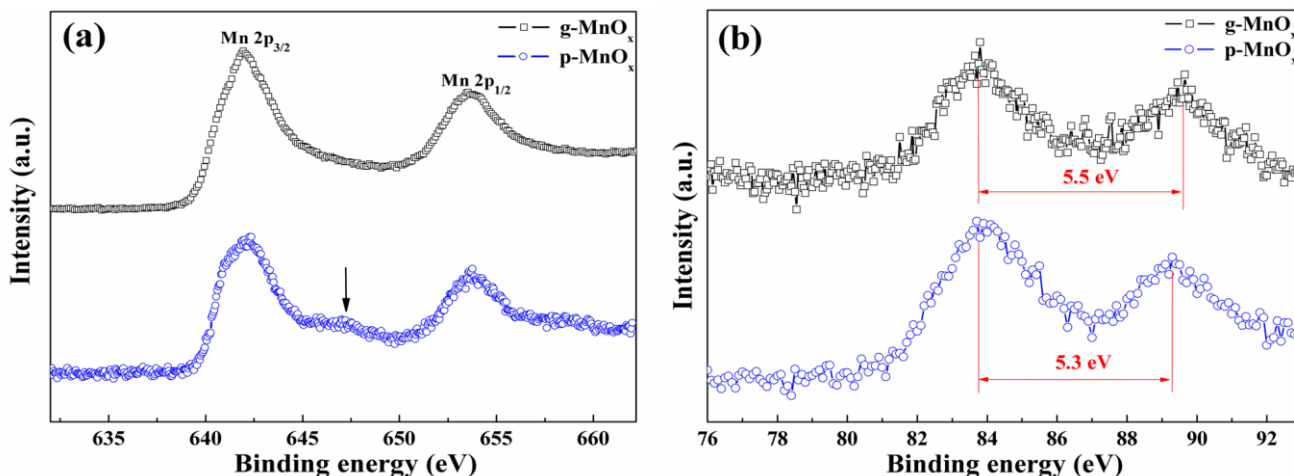


Figure 4. XPS spectra of MnO_x samples: (a) Mn 2p and (b) Mn 3s. The arrow indicates a shoulder peak

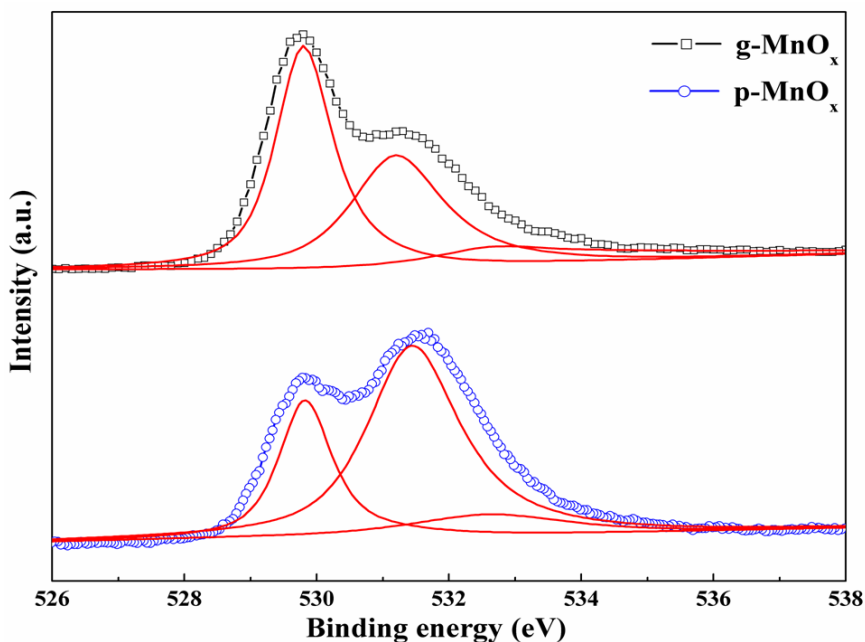


Figure 5. O 1s spectra of g-MnO_x and p-MnO_x

The multiplet peaks of Mn 3s are the result of the exchange interaction between the core level electron (3s) and the unpaired electrons in the valence band level (3d) by photoelectron ejection [31]. The multiplet splitting of Mn 3s peaks is very useful for determining oxidation state of Mn. The splitting energy (ΔE) of g-MnO_x and p-MnO_x are 5.5 eV and 5.3 eV, respectively, as shown in Fig.4

(b). According to the references [8, 31, 32], the calculated average oxidation state of Mn in g-MnO_x and p-MnO_x is about 2.5 and 2.9. The higher oxidation state of p-MnO_x is attributed to MnOOH.

The O1s XPS spectra of the MnO_x samples are shown in Fig. 5. The data of O 1s are summarized in Table 1. The O 1s spectra consist of three oxygen-containing bonds, which are Mn oxide (Mn-O-Mn) at 529.3-530.3 eV, the hydroxyl (Mn-OH) at 530.5-531.5 eV, and residual structure water (H-O-H) at 531.8-532.8 eV [33]. The amount of hydroxyl was determined to be 37.3 % (g-MnO_x) and 62.8 % (p-MnO_x), respectively. Since alkaline or proton ions diffusion in manganese oxide electrodes occur via hopping of these cation between H₂O and OH⁻ sites, the more H₂O/OH⁻ hopping sites should enhance the cation diffusion rate [1, 34, 35, 36].

Table 1. Data obtained from the O 1s XPS Spectra

Sample	g-MnO _x			p-MnO _x		
	Mn-O-Mn	Mn-OH	H-O-H	Mn-O-Mn	Mn-OH	H-O-H
BE (eV)	529.8	531.2	532.7	529.9	531.5	532.6
Area (%)	46.2	37.3	16.5	26.2	62.8	11.0

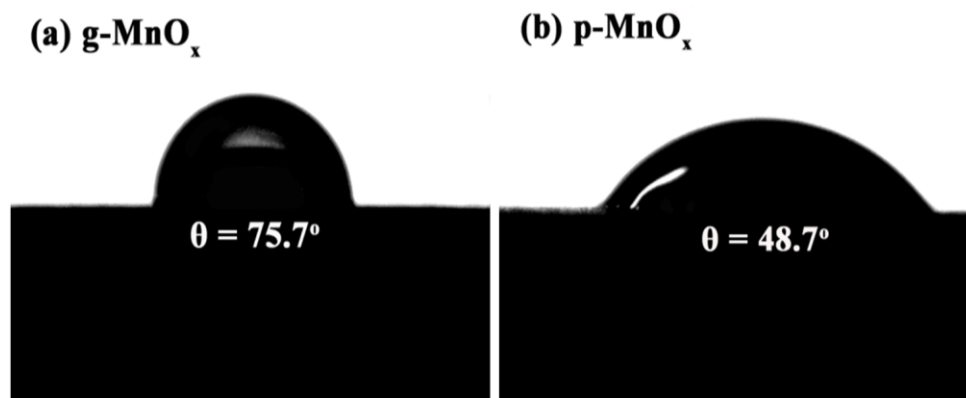


Figure 6. The contact angles of water on (a) g-MnO_x and (b) p-MnO_x

The contact angles of both MnO_x were measured in order to investigate their surface wettability [37-39]. As shown in Fig.6, the contact angle of p-MnO_x is obviously smaller than that of g-MnO_x, indicating better wettability of p-MnO_x. These results is attributed to p-MnO_x had the more compact morphology and the more amount of hydroxyl. Therefore, the better wettability of p-MnO_x is expected to enhance the cation diffusion during the charge-discharge process.

The electrochemical impedance spectra were further measured for g-MnO_x and p-MnO_x, as shown in Fig.7. In Nyquist plots, the depressed arc at high frequencies is attributed to the processes occurring at the electrode/electrolyte interface [1]. And the straight line inclined to the real axis at low frequencies consists of the impedance due to electrolytes cation diffusion within the electrode and the capacitive behavior of active materials [1].

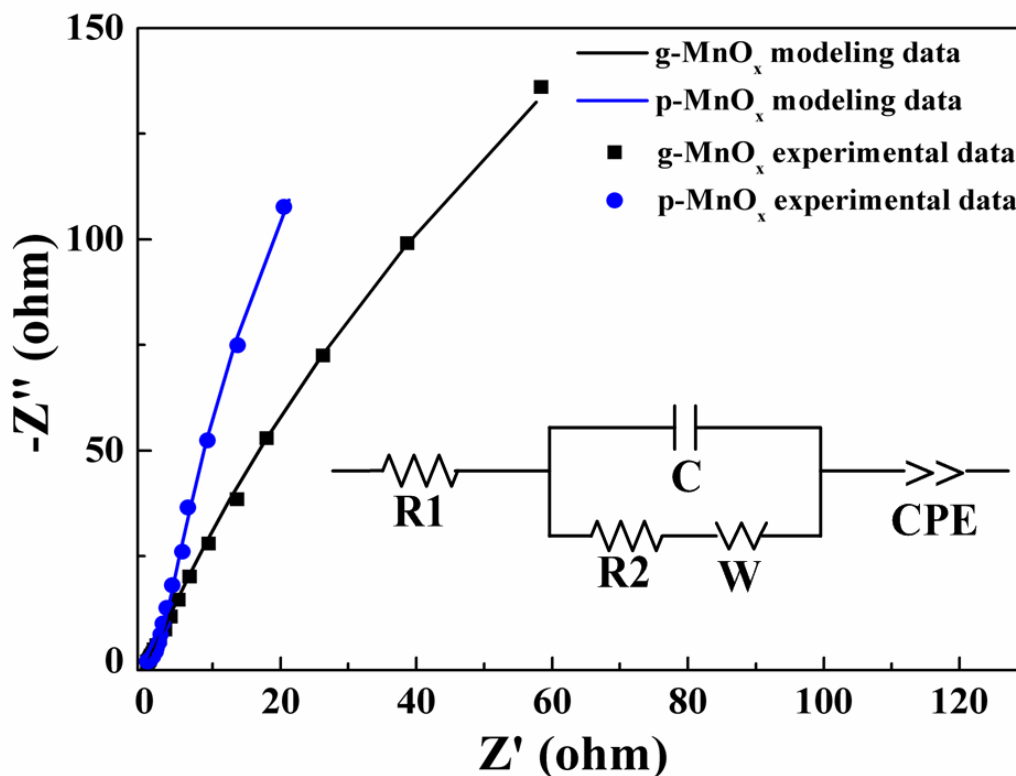


Figure 7. The Nyquist plots of g-MnO_x and p-MnO_x. And the solid lines represent the fitted data to the equivalent circuit

The impedance data were analyzed via the nonlinear least squares fitting program. The equivalent circuit consisting of five elements is shown in Fig.7. The resistance R₁ represents the ohmic resistance, which includes the resistance of the electrolyte, current collectors, electrical leads [1, 40]. R₂ and C in this model are the charge-transfer resistance and the electrical double layer capacitance at the interface of electrode/electrolyte. The Warburg impedance W is associated with the cation diffusion in the electrode. A constant phase element (CPE) is used to the non-ideal capacitive behavior at the impermeable interface [41]. The mean error of modulus is smaller than 1% in this fitting process, which represents a good fitting of the experimental data.

The modeling results show that charge-transfer resistance R₂ are g-MnO_x of 17.7 Ω cm⁻² and p-MnO_x of 3.93 Ω cm⁻², respectively. Since charge-transfer resistance corresponds to the reciprocal of the potential-dependent charge-transfer rate in the Faradic reaction [1], the less R₂ value of p-MnO_x indicates its faster charge-transfer rate. On the other hand, the Warburg impedance values are g-MnO_x of 0.0163 S sec^{0.5} cm⁻² and p-MnO_x of 0.00711 S sec^{0.5} cm⁻², respectively. The former is more 2 times higher than the latter, indicating the faster cation diffusion in p-MnO_x. This result is attributed to more H₂O/OH⁻ sites in p-MnO_x.

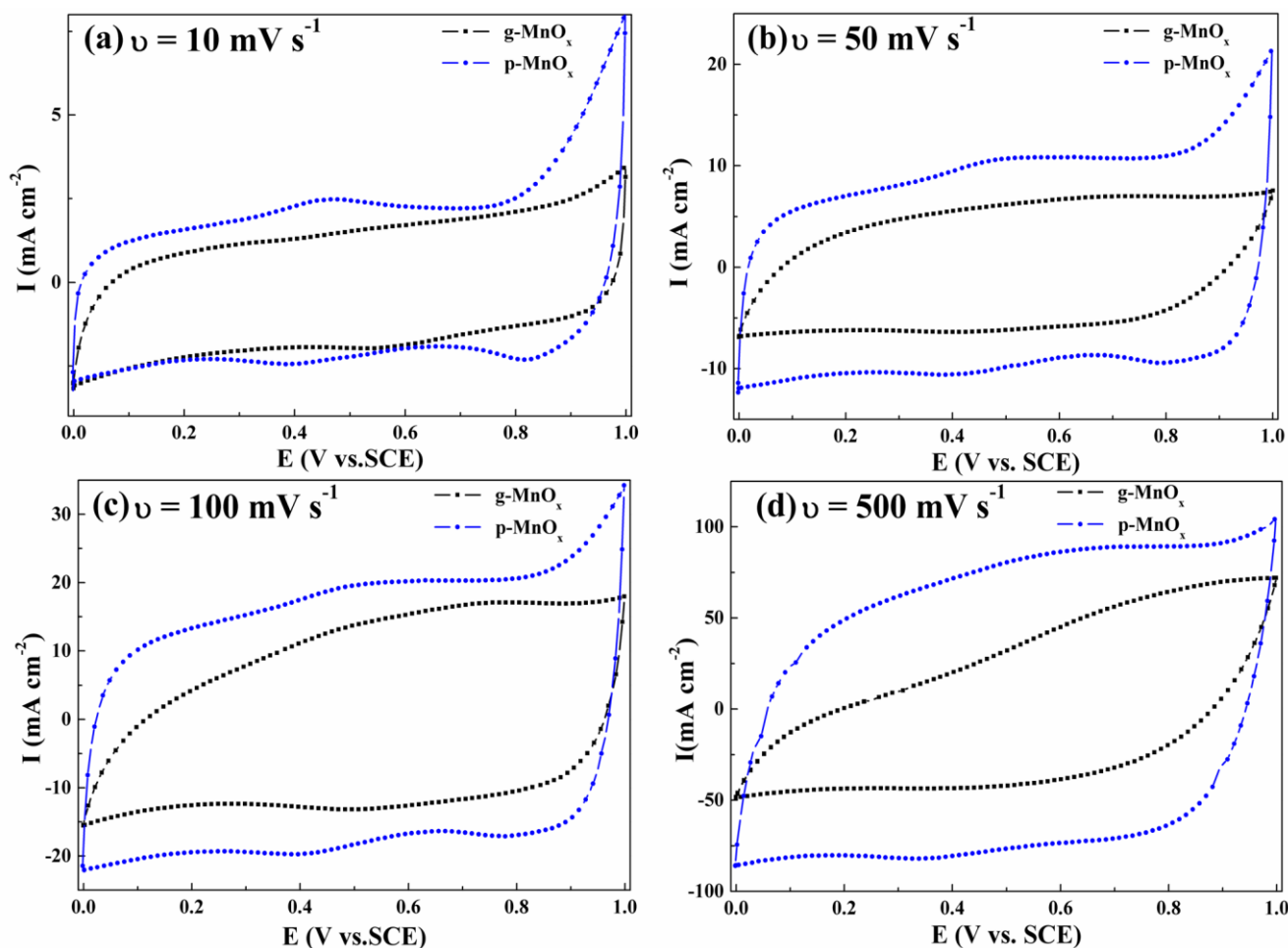


Figure 8. CV plots of g-MnO_x and p-MnO_x at the different scanning rates: (a) 10 mV s⁻¹, (b) 50 mV s⁻¹, (c) 100 mV s⁻¹ and (d) 500 mV s⁻¹

Figure 8 shows the CV curves of MnO_x samples at the scanning rate from 10 mV s⁻¹ to 500 mV s⁻¹. In Fig.8 (a), two CV curves show the rectangle-like shape, indicating the good electrochemical characteristics of both MnO_x samples. Additionally, both the CV curves present a couple of redox peaks nearly at 0.5 V (vs. SCE) [42]. This redox peaks can be assigned to the proton or alkali ions deintercalation upon oxidation and intercalation upon reduction. However, the CV curve of p-MnO_x (in Fig.8a) appears a current peak nearly at 1.0 V (vs. SCE). It was possibly attributed to the oxygen evolution reaction catalyzed by the manganese oxide [43, 44]. Fig. 8 (b – d) shows the CV curves of two MnO_x samples at other different scanning rate of 50, 100, and 500 mV s⁻¹. The CV curves of g-MnO_x deviated from the ideal capacitive behavior with the increase of scanning rate in Fig.8 (c and d). However, the CV curve of p-MnO_x still exhibits a perfectly symmetrical rectangular shape.

The specific capacitance (C) of the MnO_x is determined from the CV data [26]. The plots of C and retained ratio of C against the scanning rates are shown in Fig.9. The capacitance values of g-MnO_x and p-MnO_x were 160 F g⁻¹ and 252 F g⁻¹, respectively, as the scanning rate of 10 mV s⁻¹. The capacitance of g-MnO_x decreased to 50 F g⁻¹ when the scanning rate increased to 500 mV s⁻¹. However, the p-MnO_x retained the capacitance of 140 F g⁻¹, which was nearly 3 times than that of g-

MnO_x. The retained ratio of capacitance of g-MnO_x was 31% while that of p-MnO_x was still 56% with the scanning rate increasing from 10 mV s⁻¹ to 500 mV s⁻¹.

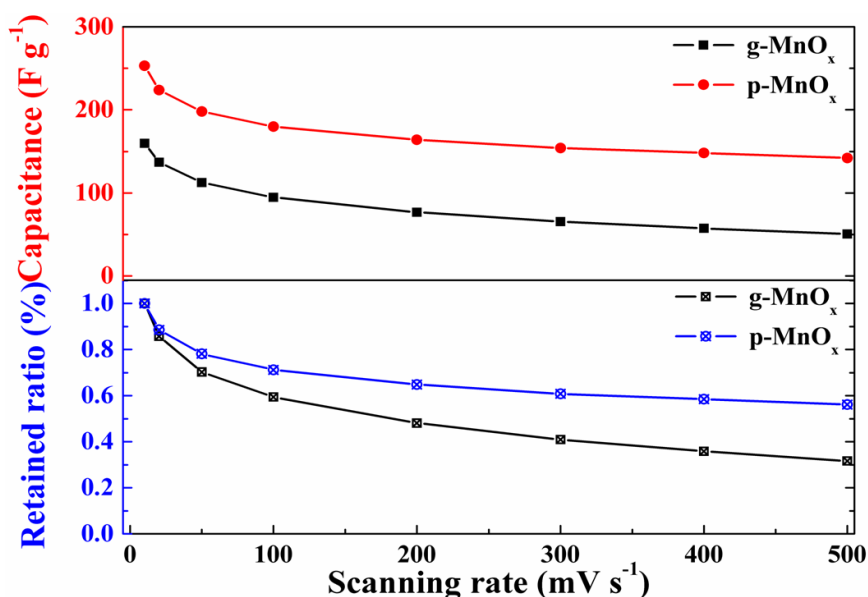


Figure 9. Specific capacitance and retained ratio of (a) g-MnO_x and (b) p-MnO_x vs. the scanning rate (v)

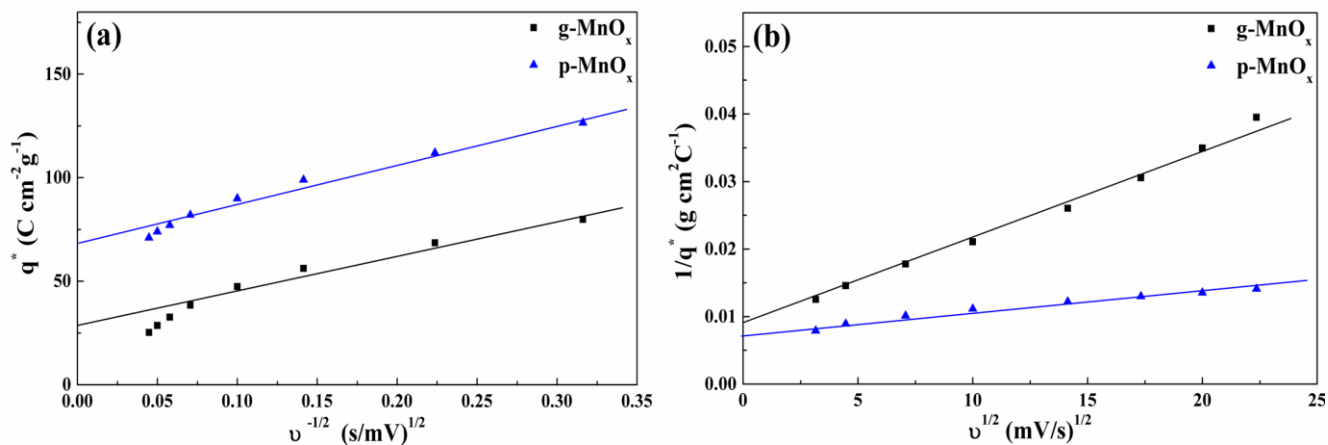


Figure 10. Variation of the voltammetric charge (q^*) with respect to the scanning rates (v): (a) the q^* vs the $1/v^{1/2}$ plot; (b) the $1/q^*$ vs $v^{1/2}$ plot

Voltammetric charges (q^*) of MnO_x samples were calculated as a function of the scanning rate. Fig. 10 (a) shows the plots of q^* as a function of the inverse of square root of the scanning rate ($v^{-1/2}$). By extrapolating $v^{-1/2}$ to infinity, outer voltammetric charge (q_0) can be calculated, which is the charge on the most accessible active surface. Fig. 10 (b) shows the plot of q^* versus square root of the scan rate ($v^{1/2}$). By extrapolating $v^{1/2}$ to zero, total voltammetric charge (q_T) can be determined, which is involved to the whole inner and outer active sites. Moreover, the difference between q_T and q_0 gives

q_I , which is related to the inner and less accessible active sites. The ratio of q_I/q_T and q_O/q_T indicate the shares of electrical charge due to inner and outer active sites, respectively. All the calculated charge values and their ratio are presented in Table 2. The q_O value of p-MnO_x is nearly three times than that of g-MnO_x. The higher q_O value of p-MnO_x should be attributed to H₂O/OH⁻ sites in p-MnO_x. Moreover, the ratio of q_O/q_T of p-MnO_x is also higher than that of g-MnO_x. At the high scanning rates, the charge storage may mainly utilize the outer active site of the electrode [1, 45]. Therefore, the p-MnO_x shows the higher capacitance at the high scanning rate.

Table 2. The estimated values of voltammetric charge on the basis of plots in Fig.10. (unit is C cm⁻² g⁻¹)

Sample	q_O	q_T	q_I	q_I/q_T	q_O/q_T
g-MnO _x	24.9	106.4	81.5	0.77	0.23
p-MnO _x	68.1	150.4	87.9	0.57	0.43

4. CONCLUSIONS

Two MnO_x films were electrodeposited by the pulse current method or galvanostatic method, respectively. The morphology of p-MnO_x was more regular and more compact than that of g-MnO_x. The structure of g-MnO_x was indexed to Mn₃O₄ while p-MnO_x showed the mixture of Mn₃O₄ and MnOOH from the XRD and Raman results. According to XPS spectra, the amount of hydroxyl in p-MnO_x was as high as 62.8%. The contact angle of p-MnO_x was obviously smaller than that of g-MnO_x, revealing the better wettability of the former. It may be attributed to the more compact morphology and the higher amount of hydroxyl of p-MnO_x. The diffusion of cation ions in p-MnO_x is easy because of its better wettability. It had been proved by the modeling results of impedance data, which showed the less charge-transfer resistance and Warburg impedance in p-MnO_x. The analysis of voltammetric charges showed that the ratio of q_O/q_T of p-MnO_x was nearly two times higher than that of g-MnO_x, indicating more accessible active sites of the former. Therefore, the better high-rate capability of p-MnO_x may be attributed to its good wettability, leading to the easier diffusion of cation ions and the more accessible active sites. These results demonstrate that pulse current prepared MnO_x film is an ideal candidate as electrode material for supercapacitor.

ACKNOWLEDGEMENTS

The authors wish to thank for the financial supports by the National High Technology Research and Development Program of China (Grant No. 2007AA03Z249) and the National Natural Science Foundation of China (Grant No. 20804030).

References

1. B.E. Conway, *Electrochemical Supercapacitors: Scientific Fundamentals and Technological Applications*, Kluwer Academic/Plenum Publisher, New York (1999).

2. J.P. Zheng, P.J. Cygan, T.R. Jow, *J. Electrochem. Soc.* 142 (1995) 2699.
3. T. Cottineau, M. Toupin, T. Delahaye, T. Brousse, D. Bélanger, *Appl. Phys. A* 82 (2006) 599.
4. A.G. Pandolfo, A.F. Hollenkamp, *J. Power Sources* 157 (2006) 11.
5. P. Simon, Y. Gogotsi, *Nat. Mater.* 7 (2008) 845-854.
6. D. Bélanger, T. Brousse, J.W. Long, *Electrochem. Soc. Interface* 17 (2008) 49.
7. W. Wei, X. Cui, W. Chen, D.G. Ivey, *Chem. Soc. Rev.* 40 (2011) 1697.
8. M. Toupin, T. Brousse, D. Bélanger, *Chem. Mater.* 14 (2002) 3946.
9. H.Y. Lee, J.B. Goodenough, *J. Solid State Chem.* 144 (1999) 220.
10. R.N. Reddy, R.G. Reddy, *J. Power Sources* 124 (2003) 330.
11. T. Abe, A. Taguchi, S. Inoue, S. Akamaru, M. Hara, K. Watanabe, *J. Alloys Compd.* 414 (2006) 137.
12. V. Subramanian, H.W. Zhu, R. Vajtai, P.M. Ajayan, B.Q. Wei, *J Phys. Chem. B* 109 (2005) 20207.
13. C.C. Hu, T.W. Tsou, *Electrochim. Acta* 47 (2002) 3523.
14. N. Nagarajan, H. Humadi, I. Zhitomirsky, *Electrochim. Acta* 51 (2006) 3039.
15. B. Babakhani, D.G. Ivey, *J. Power Sources* 195 (2010) 2110.
16. M. Gupta, D. Pinisetty, J.C. Flake, J.J. Spivey, *J. Electrochem. Soc.* 157 (2010) D473.
17. J. Wu, C.D. Johnson, Y. Jiang, R.S. Gemmen, X. Liu, *Electrochim. Acta* 54 (2008) 793.
18. J.P. Wang, Y. Xu, J. Wang, X. Du, F. Xiao, J. Li, *Synth. Met.* 160 (2010) 1826.
19. M.S. Chandrasekar, M. Pushpavanam, *Electrochim. Acta* 53 (2008) 3313.
20. G.M. Jacob, I. Zhitomirsky, *Appl. Surf. Sci.* 254 (2008) 6671.
21. H. Adelhani, M. Ghaemi, *J. Alloys Compd.* 493 (2010) 175.
22. N. Ibl, J.C. Puipe, H. Angerer, *Surf. Coat. Technol.* 6 (1978) 287.
23. C.M. Julien, M. Massot, C. Poinsignon, *Spectrochim. Acta, Part A* 60 (2004) 689.
24. F. Buciuman, F. Patcas, R. Craciun, D.R.T. Zahn, *Phys. Chem. Chem. Phys.* 1 (1999) 185.
25. E. Widjaja, J.T. Sampanthar, *Anal. Chim. Acta* 585 (2007) 241.
26. J. Jiang, A. Kucernak, *Electrochim. Acta* 47 (2002) 2381.
27. M.C. Bernard, A.H.L. Goff, B.V. Thi, S.C. Detorresi, *J. Electrochem. Soc.* 140 (1993) 3065.
28. K.W. Nam, K.B. Kim, *J Electrochem. Soc.* 153 (2006) A81.
29. B.R. Strohmeier, D.M. Hercules, *J. Phys. Chem.* 88 (1984) 4922.
30. J.K. Chang, W.T. Tsai, *J. Appl. Electrochem.* 34 (2004) 953.
31. M. Chigane, M. Ishikawa, *J. Electrochem. Soc.* 147 (2000) 2246.
32. C.H. Liang, C.S. Hwang, *J. Alloys Compd.* 500 (2010) 102.
33. D. Banerjee, H.W. Nesbitt, *Geochim. Cosmochim. Acta* 63 (1999) 3025.
34. S.C. Pang, M.A. Anderson, T.W. Chapman, *J. Electrochem. Soc.* 147 (2000) 444.
35. S.E. Chun, S.I. Pyun, G.J. Lee, *Electrochim. Acta* 51 (2006) 6479.
36. M. Ghaemi, F. Ataherian, A. Zolfaghari, S.M. Jafari, *Electrochim. Acta* 53 (2008) 4607.
37. M.S. Wu, K.H. Lin, *J. Phys. Chem. C* 114 (2010) 6190.
38. P.M. Kulal, D.P. Dubal, C.D. Lokhande, V.J. Fulari, *J Alloys Compd.* 509 (2011) 2567.
39. D.P. Dubal, D.S. Dhawale, R.R. Salunkhe, V.J. Fulari, C.D. Lokhande, *J. Alloys Compd.* 497 (2010) 166.
40. N.N. Sinha, N. Munichandraiah, *J. Solid State Electrochem.* 12 (2008) 1619.
41. D.P. Dubal, D.S. Dhawale, R.R. Salunkhe, C.D. Lokhande, *J. Electrochem. Soc.* 157 (2010) A812.
42. T. Brousse, M. Toupin, R. Dugas, L. Athouel, O. Crosnier, D. Bélanger, *J. Electrochem. Soc.* 153 (2006) A2171.
43. C.C. Hu, C.C. Wang, *J. Electrochem. Soc.* 150 (2003) A1079.
44. P. Rasiyah, A.C.C. Tseung, *J. Electrochem. Soc.* 131 (1984) 803.
45. P. Soudan, J. Gaudet, D. Guay, D. Bélanger, R. Schulz, *Chem. Mater.* 14 (2002) 1210.